Astronomy & Astrophysics

The distribution and origin of C₂H in NGC 253 from ALCHEMI

J. Holdship[1,2], S. Viti[1,2], S. Martín[3,4], N. Harada[5,6,7], J. Mangum[8], K. Sakamoto[6], S. Muller[9], K. Tanaka[10], Y. Yoshimura[11], K. Nakanishi[5,7], R. Herrero-Illana[3,12], S. Mühle[13], R. Aladro[15], L. Colzi[16,17], K. L. Emig[8,★], S. García-Burillo[14], C. Henkel[15,18], P. Humire[15], D. S. Meier[19,20], V. M. Rivilla[16,17], and P. van der Werf[1]

1. Leiden Observatory, Leiden University, PO Box 9513, 2300 RA Leiden, The Netherlands
   e-mail: holdship@strw.leidenuniv.nl
2. Department of Physics and Astronomy, University College London, Gower Street, London WC1E 6BT, UK
3. European Southern Observatory, Alonso de Córdova, 3107, Vitacura, Santiago 763-0355, Chile
4. Joint ALMA Observatory, Alonso de Córdova, 3107, Vitacura, Santiago 763-0355, Chile
5. National Astronomical Observatory of Japan, 2-21-1 Osawa, Mitaka, Tokyo 181-8588, Japan
6. Institute of Astronomy and Astrophysics, Academia Sinica, 11F of AS/NTU Astronomy-Mathematics Building, No. 1, Sec. 4, Roosevelt Rd, Taipei 10617, Taiwan
7. Department of Astronomy, School of Science, The Graduate University for Advanced Studies (SOKENDAI), 2-21-1 Osawa, Mitaka, Tokyo 181-1855, Japan
8. National Radio Astronomy Observatory, 520 Edgemont Road, Charlottesville, VA 22903-2475, USA
9. Department of Space, Earth and Environment, Chalmers University of Technology, Onsala Space Observatory, 43992 Onsala, Sweden
10. Department of Physics, Faculty of Science and Technology, Keio University, 3-14-1 Hiyoshi, Yokohama, Kanagawa 223–8522, Japan
11. Institute of Astronomy, Graduate School of Science, The University of Tokyo, 2-21-1 Osawa, Mitaka, Tokyo 181-0015, Japan
12. Institute of Space Sciences (ICE, CSIC), Campus UAB, Carrer de Magrans, 08193 Barcelona, Spain
13. Argelander-Institut für Astronomie, Universität Bonn, Auf dem Hügel 71, 53121 Bonn, Germany
14. Observatorio Astronómico Nacional (OAN-IGN), Observatorio de Madrid, Alfonso XII, 3, 28014 Madrid, Spain
15. Max-Planck-Institut für Radioastronomie, Auf dem Hügel 69, 53121 Bonn, Germany
16. Centro de Astrobiología (CSIC-INTA), Ctra. de Ajalvir Km. 4, Torrejón de Ardoz 28850, Madrid, Spain
17. INAF-Osservatorio Astrofisico di Arcetri, Largo Enrico Fermi 5, 50125 Florence, Italy
18. Astron. Dept., Faculty of Science, King Abdulaziz University, PO Box 80203, Jeddah 21589, Saudi Arabia
19. New Mexico Institute of Mining and Technology, 801 Leroy Place, Socorro, NM 87801, USA
20. National Radio Astronomy Observatory, PO Box O, 1003 Lopezville Road, Socorro, NM 87801, USA

ABSTRACT

Context. Observations of chemical species can provide insights into the physical conditions of the emitting gas however it is important to understand how their abundances and excitation vary within different heating environments. C₂H is a molecule typically found in PDR regions of our own Galaxy but there is evidence to suggest it also traces other regions undergoing energetic processing in extragalactic environments.
Aims. As part of the ALCHEMI ALMA large program, we map the emission of C₂H in the central molecular zone of the nearby starburst galaxy NGC 253 at 1.6″ (28 pc) resolution and characterize it to understand its chemical origins.
Methods. We used spectral modeling of the $N = 1-0$ through $N = 4-3$ rotational transitions of C₂H to derive the C₂H column densities towards the dense clouds in NGC 253. We then use chemical modeling, including photodissociation region (PDR), dense cloud, and shock models to investigate the chemical processes and physical conditions that are producing the molecular emission.
Results. We find high C₂H column densities of $\sim 10^{15}$ cm^{-2} detected towards the dense regions of NGC 253. We further find that these column densities cannot be reproduced if it is assumed that the emission arises from the PDR regions at the edge of the clouds. Instead, we find that the C₂H abundance remains high even in the high visual extinction interior of these clouds and that this is most likely caused by a high cosmic-ray ionization rate.

Key words. galaxies: individual: NGC 253 – astrochemistry – submillimeter: galaxies – radiative transfer

1. Introduction

Observations of chemical species provide a wealth of information about the physical conditions of astrophysical objects. However, in order to get the most information from a particular observation, it is important to understand the chemistry and excitation of molecules and related atomic species under differ-

ent conditions. Whether the species under study is a classical dense gas tracer like CS (e.g., van der Tak et al. 2000) or more characteristic of photon-dominated regions (PDRs) such as C⁺, many of the most useful tracers are those whose relationships to physical parameters of interest are well understood.

Within the Milky Way, ethynyl (C₂H) is a typical photodissociation region (PDR) tracer as its chemistry is strongly linked to C⁺ (Meier & Turner 2005). It is observed at low

---

fractional abundances ($\sim 10^{-10}$) in dense clouds (Wootten et al. 1980; Watt et al. 1988) and enhanced to $\sim 10^{-8}$ in low density gas (Turner et al. 1999; Lucas & Liszt 2000), where UV photons can penetrate and ionize C which is a key reactant in a chain of reactions that form C_2H. Whilst C_2H is also abundant in these environments in extragalactic objects (e.g., Aladro et al. 2011, 2015), there is an indication that it may be tracing more than just PDR regions in those extragalactic environments (García-Burillo et al. 2017).

A previous work focused on the Seyfert galaxy NGC 1068 (García-Burillo et al. 2017) indicated that C_2H could be a tracer of the interface between high energy outflows and the ambient gas in a galaxy. The starburst ring of this galaxy showed a typical C_2H abundance ($\sim 10^{-8}$) similar to that found in diffuse clouds in Galactic environments. However, a larger, more extended component of gas had an abundance of $\sim 10^{-6}$ in the region between the molecular disk and ionized gas outflow. Chemical modeling efforts showed this larger abundance was only consistent with the short, early stages of models where some energetic process such as high cosmic ray ionization or shocks enhanced the C_2H abundance. It was theorized in that work that the interface between an outflow and ambient gas would create an environment where unprocessed gas would continually be replenished and subjected to energetic processing. This could create a pseudo-steady state where the C_2H abundance is stable at the high value found in the early stages of simple shock models.

It is possible therefore that C_2H is a good tracer of molecular gas that is undergoing energetic processing and, more specifically, of the interface between active galactic nuclei (AGN) driven outflows and their environment. This would make it a useful tool for extragalactic observations. However, this must be tested against other galaxies. Moreover, only one multiplet of C_2H was observed towards NGC 1068 and so additional transitions must be observed to assess excitation conditions and thus give a clearer picture.

NGC 253 is a prototypical starburst galaxy that hosts several large (~ 30 pc), dense ($\sim 10^5$ cm^{-3}) clouds which are well studied (e.g., Sakamoto et al. 2011; Leroy et al. 2018). Though similar in size to giant molecular clouds (GMCs) in the Milky Way, they are orders of magnitude more massive and have higher velocity dispersions (Leroy et al. 2015). NGC 253 was the chosen target of the ALCHEMI ALMA large program (Martín et al. 2021), which aimed at obtaining the most complete extragalactic molecular inventory in the central molecular zone of a starburst galaxy at a spatial resolution of tens of parsecs. NGC 253 also has a starburst driven outflow which can be observed at X-ray wavelengths (Dahlem et al. 1998) and in molecular emission (Bolatto et al. 2013; Krieger et al. 2019). This outflow may lead to a chemical environment similar to the AGN driven outflow of NGC 1068.

In summary, NGC 253 presents an interesting test case for the scenario proposed and modeled for NGC 1068. The star-forming regions of NGC 253 should present C_2H emission similar to that found in the starburst ring of NGC 1068. More importantly, if enhanced C_2H abundances are observed along the outflow then the chemical origin must be due to some commonality between the outflows from both galaxies. Alternatively, if enhanced abundances are not observed, this would indicate a different chemical composition between starburst-driven outflows and AGN-driven outflows.

To investigate this, images of multiple transitions of C_2H in the central molecular zone (CMZ) of NGC 253, as well as calculations of the column density and fractional abundance are presented. In Sect. 2, the observations and ALCHEMI large program are described. In Sect. 3, the C_2H emission distribution and column densities are discussed. In Sect. 4, average fractional abundances are interpreted through chemical models.

2. Observations and image processing

2.1. Observations

The analysis presented in this article makes use of the data collected by the ALMA ALCHEMI large program, which is an unbiased spectral survey of NGC 253 covering the full ALMA spectral bands 3 through 7. The ALCHEMI program and all observational details are described extensively in Martín et al. (2021). A summary of ALCHEMI survey details pertinent to the C_2H data presented in this article is given here.

NGC 253 was observed toward a nominal phase center of $\alpha = 00^h47^m33.26^s$, $\delta = -25°17'17.7''$ (ICRS). Observations were configured to cover a common rectangular area of $50'' \times 20''$ with a position angle of $65°$ (East of North). The spectral configuration for the ALCHEMI Survey of NGC 253 was configured with 47 receiver tunings; each comprising four 1.875 GHz spectral windows. All tunings were imaged to a shared beam size of $1\rlap{.}''6$ and the maximum recoverable scale was $15''$[1]. At a distance of 3.5 Mpc (Rekola et al. 2005), these correspond to linear scales of 28 and 250 pc, respectively. Within the ALCHEMI frequency coverage, four multiplets of C_2H transitions namely $N = 1-0$, $2-1$, $3-2$, and $4-3$ were observed. This includes 39 hyperfine transitions across ALMA bands 3, 5, 6, and 7 and these are listed in Table 1.

The datacubes used in this work have been made available as part of the public release of the ALCHEMI data. The FITS files associated with the B3a, B5d, B6g, and B7o science goals were used for this work each covering a single multiplet from $N = 1-0$ to $N = 4-3$.

2.2. Data processing

We loaded and processed the FITS files using Astropy and Spectral Cube (Astropy Collaboration 2013, 2018). Standard routines from those packages were then used to produce moment 0 maps. The velocity ranges for those maps are given in Table 2 and were chosen so that they contain all the C_2H lines but excluded any strong lines from other species that may contaminate the maps. This was informed by local thermodynamic equilibrium (LTE) modeling of the ALCHEMI project's ALMA compact array data of the region (Martín et al. 2021) that provided both the velocity ranges that would cover all expected C_2H emission and the line intensities of possible contaminating lines. Only the $N = 3-2$ transition was likely to be contaminated and, as a result, we chose a velocity interval that excluded a hyperfine component with frequency 261.834 GHz in order to remove the 7_6-6_5 line of SO. The spectral modeling performed in this work (Sect. 3.3) predicted negligible emission from the omitted C_2H line and verified that the chosen velocity ranges contained all other C_2H emission.

---

[1] The maximum recoverable scale corresponds to the size of the largest structure that can be observed with a given array configuration of an interferometer. In practice, it can be estimated as λ/B_{min}, where λ is the wavelength and B_{min} is the length of the shortest projected baseline during the observations. (See also https://almascience.nrao.edu/documents-and-tools/cycle8/alma-technical-handbook/view.)

Table 1. C$_2$H transitions covered by the ALCHEMI large program's observations taken from JPL (Pickett 1998).

Frequency/GHz (GHz)	Quantum numbers	$\log_{10}(A_{ij})$ $\log_{10}(\mathrm{s}^{-1})$	E_U (K)
	N = 1−0		
87.284	$J = 3/2-1/2, F = 1-1$	−6.43	4.2
87.317	$J = 3/2-1/2, F = 2-1$	−5.66	4.2
87.329	$J = 3/2-1/2, F = 1-0$	−5.74	4.2
87.402	$J = 1/2-1/2, F = 1-1$	−5.74	4.2
87.407	$J = 1/2-1/2, F = 0-1$	−5.65	4.2
87.447	$J = 1/2-1/2, F = 1-0$	−6.42	4.2
	N = 2−1		
174.663	$J = 5/2-3/2, F = 3-2$	−4.67	12.6
174.668	$J = 5/2-3/2, F = 2-1$	−4.71	12.6
174.722	$J = 3/2-1/2, F = 2-1$	−4.78	12.6
174.728	$J = 3/2-1/2, F = 1-0$	−4.93	12.6
174.733	$J = 3/2-1/2, F = 1-1$	−5.13	12.6
174.807	$J = 3/2-3/2, F = 2-2$	−5.41	12.6
	N = 3−2		
262.004	$J = 7/2-5/2, F = 4-3$	−4.11	25.2
262.006	$J = 7/2-5/2, F = 3-2$	−4.13	25.2
262.064	$J = 5/2-3/2, F = 3-2$	−4.15	25.2
262.067	$J = 5/2-3/2, F = 2-1$	−4.19	25.2
262.078	$J = 5/2-3/2, F = 2-2$	−5.06	25.2
262.208	$J = 5/2-5/2, F = 3-3$	−5.24	25.2
	N = 4−3		
349.337	$J = 9/2-7/2, F = 5-4$	−3.72	41.9
349.338	$J = 9/2-7/2, F = 4-3$	−3.73	41.9
349.398	$J = 7/2-5/2, F = 4-3$	−3.74	41.9
349.400	$J = 7/2-5/2, F = 3-2$	−3.76	41.9

Table 2. Velocity limits used to produce the moment 0 maps for each C$_2$H multiplet.

Multiplet	Transition frequency (GHz)	Velocity range (km s^{-1})
N = 1−0	87.407	−185 to 370
N = 2−1	174.663	−220 to 380
N = 3−2	262.004	−185 to 310
N = 4−3	349.337	−185 to 415

Notes. Velocities are given according to the radio convention using the frequency of the highest A_{ij} in each multiplet. The wide ranges account for multiple components rather than being determined by line width.

We also extracted spectra using Spectral Cube and used the package's unit conversion to convert the extracted spectra to units of Kelvin. We estimated the noise value for any given spectrum from the mean difference between the median value and all channels lower than the median. This is effectively taking the variance whilst excluding channels above the average as they are "contaminated" by signal. Where the spectra were extracted from multiple pixels, such as in the GMCs (Sect. 3.1), a median stack of the individual pixel spectra was taken.

2.3. Spectral modeling

C$_2$H is a molecule with hyperfine structure that, together with the broad velocity distributions in the data, produces spectra with large numbers of blended lines. Furthermore, the complex dynamic situation in NGC 253 gives rise to multiple, blended emitting components (Krieger et al. 2020). As such, a spectral model is required to disentangle the emission.

In this work, we used SpectralRadex[2] to model the spectra. This is a Python package that creates model spectra from RADEX using a formalism described in Appendix A. Briefly, it contains a wrapper to run RADEX (van der Tak et al. 2007) in order to obtain the excitation temperature and the optical depth at the line centre of every modeled transition. The package then produces model spectra by assuming that each transition follows a Gaussian line profile described by the central velocity and FWHM. It has been benchmarked against the RADEX based spectral model in CASSIS[3] (Vastel et al. 2015) for a wide variety of test cases and each best fit presented in this work has been replicated in CASSIS. Collisional rates between C$_2$H and ortho and para H$_2$ were used (Dagdigian 2018) to produce the RADEX outputs assuming an ortho to para ratio of 3:1. These cover a temperature range of 10−300 K and were taken from the LAMDA database[4] (Schöier et al. 2005).

3. Results

3.1. Distribution of C$_2$H

In Fig. 1, the integrated emission of each observed group of C$_2$H hyperfine transitions is shown. Each group of transitions follows broadly the same distribution with the $N = 2-1$ group being the brightest. Most strikingly, the majority of the C$_2$H emission does not appear to follow the full extent of the outflow traced in CO by Krieger et al. (2019). The $N = 1-0$ emission traces the SW streamer which has been observed in CO (Walter et al. 2017) (see Fig. 2) but the outflow is otherwise not apparent.

The majority of the emission arises from five clumps that are therefore the focus of this work. The position of each clump corresponds to one of the giant molecular clouds (GMCs) identified in Leroy et al. (2015) and so their numbering system is adopted. However, it should be noted that, at higher resolution, GMC 4, 5 and 6 have been resolved into smaller structures and consist of several dense objects that are blended in larger beams (Ando et al. 2017; Mangum et al. 2019).

The positions of the clumps were first approximately identified by eye and then five 2D dimensional Gaussian distributions were fit to the $N = 2-1$ moment 0 map using those positions as initial guesses for the central coordinates. The sizes and central positions of the Gaussians were then simultaneously adjusted to minimize the discrepancy between their sum and the moment 0 map. This allowed the positions and sizes of the five clumps to be fit, taking into account the overlap between them. These five objects are the brightest GMCs in the region when observed in both the continuum and the CO 2−1 transition (Sakamoto et al. 2011).

In order to approximate an angular size for the GMCs, the FWHM of a symmetric Gaussian with the same solid angle as the fitted 2D Gaussian was calculated. This was taken to be the convolved size of the source in the beam ($\Omega_{\mathrm{S*B}}$). From this, the filling factor can be calculated as

$$\eta_{\mathrm{ff}} = \frac{\Omega_{\mathrm{S*B}} - \Omega_{\mathrm{B}}}{\Omega_{\mathrm{S*B}}}, \tag{1}$$

---

[2] https://spectralradex.readthedocs.io
[3] http://cassis.irap.omp.eu/
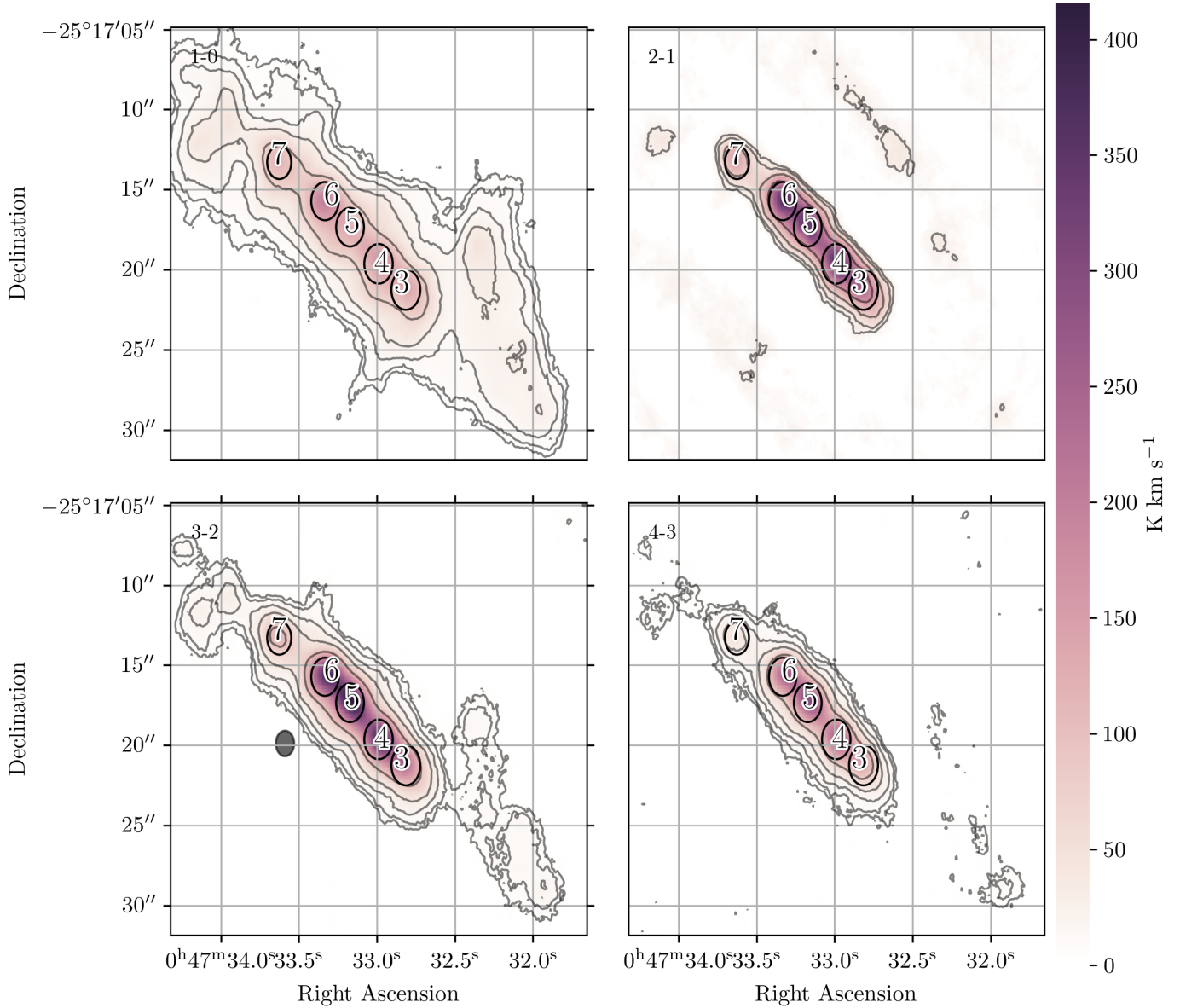[4] https://home.strw.leidenuniv.nl/~moldata/

Fig. 1. Integrated emission maps of C₂H in NGC 253. The beam size for all panels is 1.6″ and is shown in the *bottom left panel*. Since the beam size is shared, the wider spatial distribution of the $N = 1-0$ emission is not caused by a beam size effect. Contours at the 3, 5, 10, 20 and 50σ level are drawn in black. The noise levels in order of increasing N are 1.4, 8.5, 2.0 and 1.6 K km s⁻¹. Each ellipse shows the position and size of the Gaussian fits to the four individual clumps described in Sect. 3.1. The numbers indicate the position of the GMCs in Leroy et al. (2015).

which is a simple substitution of Ω_{S*B} into the more standard $\frac{\Omega_s}{\Omega_{S*B}}$ (Martín et al. 2019) where Ω_B is the solid angle of the beam. These filling factors were used to correct the intensity of all spectra extracted from the GMCs in this work. The positions of the GMCs, their convolved angular sizes and the filling factors are given in Table 3.

Whilst most emission is confined to the GMCs, there is also extended emission over the CMZ. In Fig. 1, it is clear the emission above the 3σ level generally extends far past the GMCs, covering the CMZ region traced by other molecules (Sakamoto et al. 2011). The CMZ emission is strongest and has the largest extent in the $N = 1-0$ emission. All beam sizes are 1.6″ so the wider spatial distribution of the $N = 1-0$ emission is not a beam size effect. Therefore, there must be a gas component present that is sufficiently different in nature to the GMCs to excite $N = 1-0$ emission more strongly than the others. Figure 2

shows the extent of this emission which is referred to as the extended emission going forward.

3.2. Characterizing the extended emission

The focus of this work is on the C₂H emission from the GMCs. However, one would expect some contribution from the extended emission to any spectra extracted from the GMC positions because the map in Fig. 2 shows the CMZ surrounds the GMCs. Moreover, preliminary modeling work showed that the $N = 1-0$ and $N = 4-3$ lines could not be simultaneously fit by a single component in any spectrum.

In order to attempt to reduce the degeneracy inherent in fitting multiple gas components to a spectrum, the extended emission was characterized first to obtain constraints on possible values that could be used in the GMC fit. In Fig. 3,
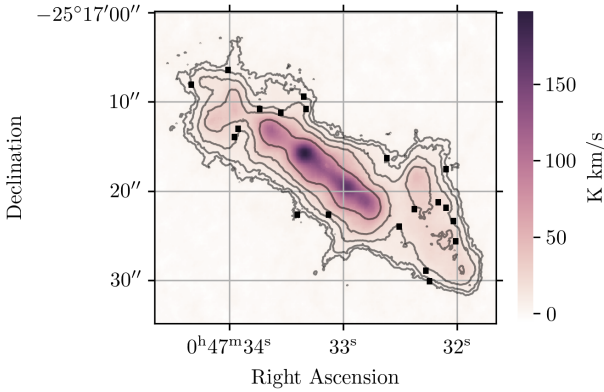
Fig. 2. Integrated emission map of the C$_2$H $N = 1-0$ multiplet as in Fig. 1 but showing the full extent of the emission. Contours are shown at the 3, 5, 10, 20 and 50σ levels for noise level of $\sigma = 1.5$ K km s^{-1}. Black squares indicate the positions sampled for spectra in Fig. 3.

Table 3. Details of the GMCs observed in C$_2$H and studied in this work including co-ordinates, convolved size and beam filling factor.

GMC	RA/''	Dec/''	Θ_{S*B}/''	η_{ff}
3	32.826	−21.399	2.5	0.58
4	33.000	−19.783	2.5	0.58
5	33.183	−17.498	2.4	0.56
6	33.344	−15.872	2.4	0.55
7	33.637	−13.446	2.1	0.42

Notes. Coordinates are given as arcsecond offsets from $00^h47^m00^s$, $-25°17''00''$.

spectra from random positions throughout the extended region are shown. They have been resampled to common frequency bins and median stacked without velocity shifting. The positions from which they were extracted are indicated by black squares in Fig. 2.

These spectra are not directly analysed and are meant only to show the general trend of the extended emission from the CMZ. They are strongest in the $N = 1-0$ transition and become successively weaker at higher N, with the $2-1$ line being anomalously weak. This same trend can be seen in the moment 0 maps. Thus the properties of the CMZ gas can be constrained by demanding the emission predicted by radiative transfer model follows this trend.

A large grid of RADEX models was run in which the gas density, column density and gas temperature were varied. The trialled ranges of these variables are given in Table 4. The parameter space that would be appropriate for the extended emission was then found by utilising two simple constraints. First, all models where the peak $N = 1-0$ emission was less than 0.03 K were rejected because this would be less than three times the rms noise in the CMZ spectra. Second, any model where the $N = 1-0$ emission was not the strongest of the four detected lines was also rejected as the $N = 1-0$ lines are the brightest part of the extended emission. The parameter values of the remaining models define a parameter space that would be appropriate for the extended emission.

Table 4 gives the parameter ranges that conformed to the above constraints. This is also illustrated in Fig. 4 where the points indicate a set of parameters that match our constraints. From this figure, relationships between the variables can be seen. Given the weak constraints from the data used for this procedure, the parameters are not well constrained. In particular, the column density is essentially unconstrained as the relative strengths of lines is all that was used rather than the absolute values.

However, the constraints on the gas properties are important. The gas must be at a low density between 3.5×10^3 cm^{-3} and 1.7×10^4 cm^{-3}. It must also be warm as all models that fit our loose constraints have a gas temperature >50 K. This is similar to the PDR regions in which C$_2$H is observed in our own Galaxy (Pilleri et al. 2013; Cuadrado et al. 2015). Further, these limits can be used to inform the GMC modeling in Sect. 3.3, breaking the degeneracy inherent in fitting multiple gas components to a single spectrum.

3.3. Characterizing the GMCs

In order to model the GMC spectra, two gas components were used for each GMC. The first was limited to the constrained range of parameters given in Table 4 to allow for the extended emission contributing to the spectra. The second component simply had to have a larger density than the extended emission and represents the component from the GMC itself.

The fits were performed via a Bayesian inference procedure in which emcee (Foreman-Mackey et al. 2013) was used to evaluate the posterior distribution of the parameters assuming flat priors and a Gaussian likelihood. The error on each channel was taken to be the spectral noise and an absolute calibration uncertainty of 15% (see Martín et al. 2021 for details) of the channel intensity added in quadrature. Thus the reported most likely values are equivalent to those found through χ^2 minimization but the reported uncertainties are based on the probability distribution of the parameters given the measured spectra.

One special case was GMC 5 for which the best fit is shown in Fig. 5. This GMC very clearly has two distinct velocity components, possibly due to the fact that GMC 5 actually comprises at least four clumps with varying gas velocities (Ando et al. 2017). Despite this known substructure, we chose to fit the two velocity components that are apparent in the data; one with a central velocity of less than 200 km s^{-1} and one with a velocity larger than 200 km s^{-1}. Since the CMZ contaminates both, we further add two low density components. This gives a total of four components: one low density and one high density for each velocity range.

The spectra fits in Fig. 5 and Appendix B show that the assumption that the extended emission is contaminating the GMC spectra are justified. The results of the fitting in these figures show the $N = 1-0$ line is dominated by the extended emission component as expect from the fact the extended emission is brightest in this component.

The focus of this work is on the GMC emission and so only the values of the high density component are reported in the following sections. The parameters describing the extended components are therefore treated as nuisance parameters and are simply marginalized over. As a result, the reported uncertainty on the GMC component parameters contains the uncertainty from the degeneracy inherent in fitting multiple components.

3.3.1. C$_2$H abundance

The inferred properties of the GMCs, excluding the extended emission, are presented in Table 5. For each GMC, the single best fit value of each parameter is presented along with the interval containing 67% of the probability density of the marginalized
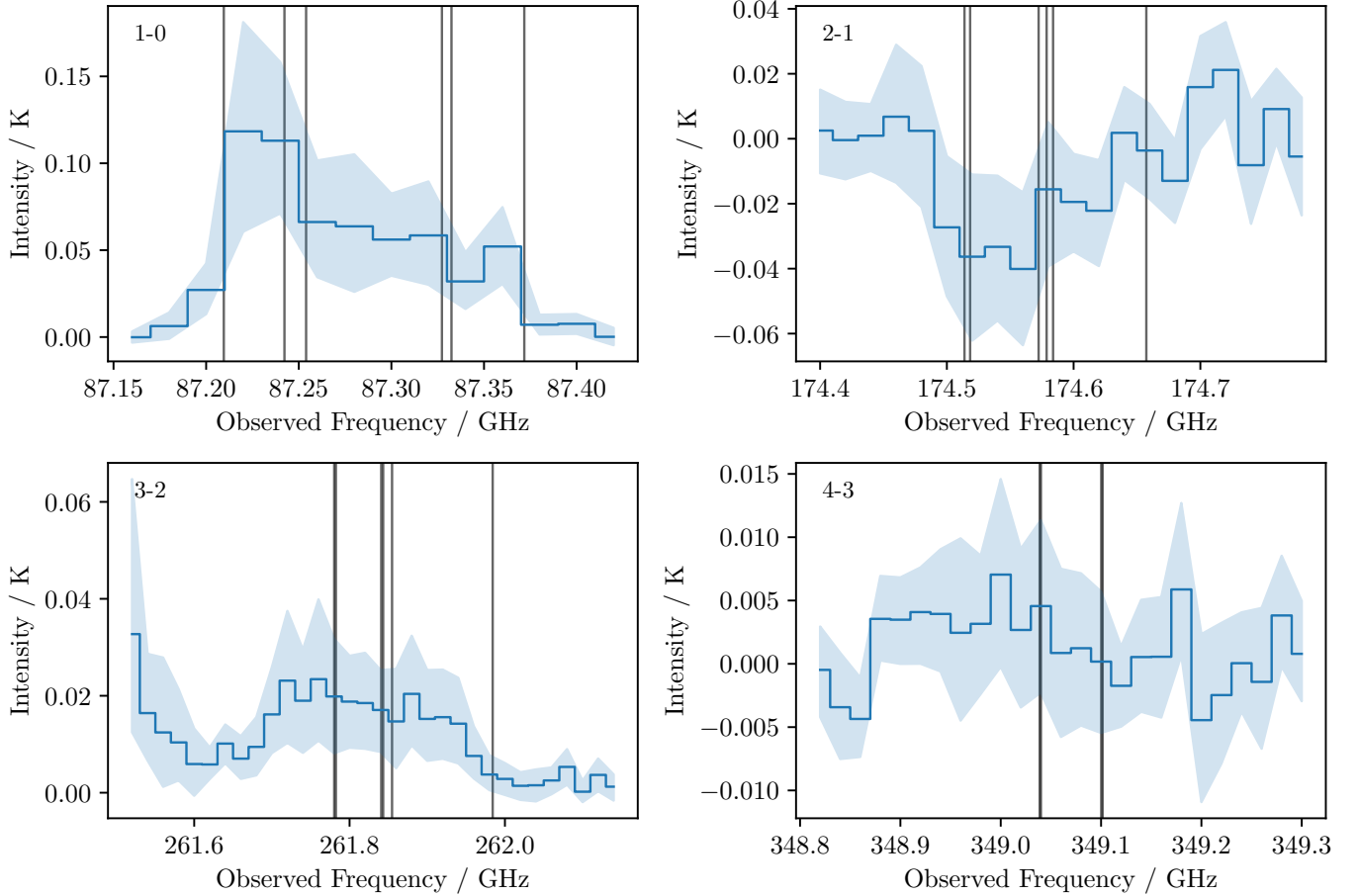
Fig. 3. Median stack of all spectra sampled from the extended region of the CMZ. The median is shown as a line and the shaded region gives the 95% confidence interval on this value. The black squares in Fig. 2 indicate the positions from which spectra were extracted for this composite spectrum. The black lines indicate the positions of the C_2H components in each N transition, Doppler shifted by $255\,km\,s^{-1}$, the LSR velocity of NGC 253.

Table 4. RADEX parameters used to constrain the gas properties of the extended emission component.

Variable	Trialled range	Constrained range
Gas density/cm^{-3}	10^2-10^8	$3.5 \times 10^3 - 1.7 \times 10^4$
$N(C_2H)$/cm^{-2}	$10^{12}-10^{18}$	$10^{13}-10^{18}$
Gas temperature/K	$10-300$	$50-300$

posterior distribution of that parameter. This can be thought of as a 1σ interval. The RADEX derived column density of C_2H is fairly uniform across the GMCs, each having a best fit value in the range $10^{15}-10^{16}\,cm^{-2}$.

However, if the total H_2 column density of the cloud is considered, the C_2H abundances are more varied. Using the H_2 column density measured from the continuum by Mangum et al. (2019) towards each GMC and assuming the H_2 and C_2H trace the same gas, we calculate the C_2H fractional abundances which are given in Table 6. These vary in the range $3.6 \times 10^{-10}-1.7 \times 10^{-8}$.

3.3.2. Gas properties

In general the temperature of the gas is poorly constrained by our C_2H data, with the marginalized posteriors for the temper-
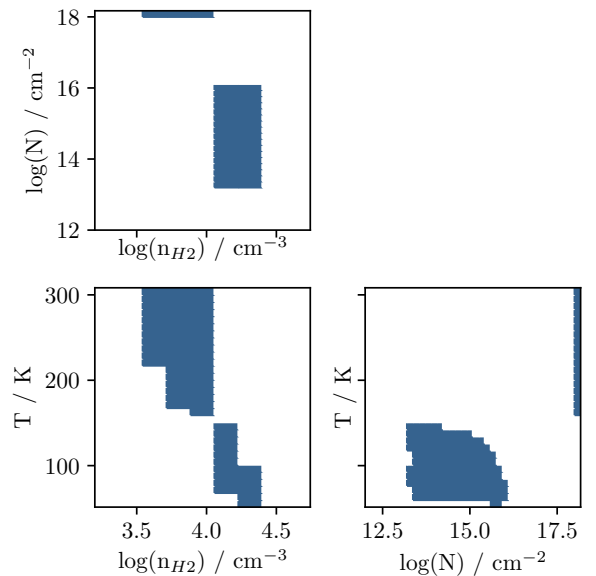

Fig. 4. Model parameters that fit constraints from the extended emission of the CMZ. Each point represents the parameters of a model where the $N = 1-0$ line was the strongest line and was above noise.

ature being approximately flat in the range $50-300\,K$. This is to be expected given that the highest upper state energy of the
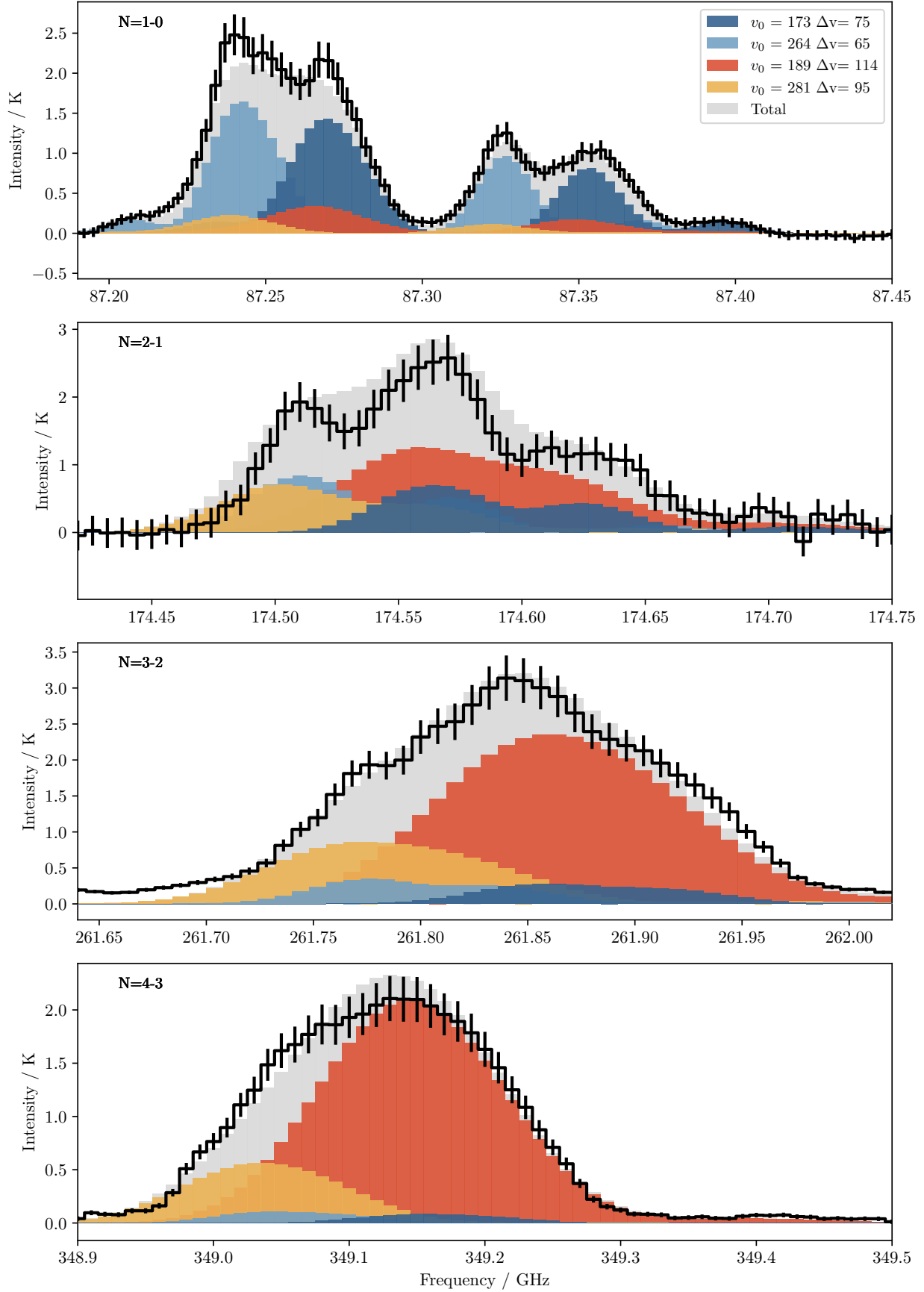
Fig. 5. Best fit model for GMC 5. The black trace shows the measured spectra with error bars. The histograms show the spectral model components in colour and their total in grey. The legend gives the central velocity (V_0) and linewidth (ΔV) of each component. The two blue components are the low density CMZ contribution and the others are the high density GMC components.

Table 5. Parameter estimates with 1σ range from the spectral model fitting to each GMC.

GMC	$N/10^{15}$ cm^{-2}		$n_{\mathrm{H2}}/10^5$ cm^{-3}		$T_{\mathrm{kin}}/$K		$V/$km s^{-1}		$\Delta V/$km s^{-1}	
Component	Best fit	Range	Best fit	Range	Best fit	Range	Best fit	Range	Best fit	Range
7	1.5	1.1–1.5	6.9	1.5–12.1	31.7	27.7–109.6	173.8	171.9–175.4	84.1	81.6–90.1
6	3.7	3.5–14.1	1.2	0.9–4.0	–	>70.3.9	182.5	181.0–185.6	68.4	65.9–78.0
5 – low V	4.0	1.9–4.1	1.1	1.1–2.6	–	>109.4.5	189.0	167.3–194.1	113.8	90.2–120.0
5 – high V	1.5	1.0–3.7	2.8	1.0–18.2	–	>29.0	280.7	228.7–288.4	94.8	80.7–140.9
4	4.2	3.9–10.8	1.0	0.3–1.5	–	>130.3	246.3	245.1–251.6	80.8	76.8–80.9
3	2.1	1.9–2.5	1.1	0.9–4.8	–	>46.9	282.0	281.2–282.9	58.9	57.4–61.2

Notes. Where the marginalized probability distribution for a parameter becomes approximately flat above a certain value, no best fit value is given and lower limits are provided.

Table 6. Most likely fractional abundance of C_2H and likely bounds.

GMC	$X(C_2H)$	Lower bound	Upper bound	$N_{\mathrm{H2}}/10^{23}$ cm^{-2}
7	1.1×10^{-08}	6.6×10^{-09}	1.5×10^{-08}	1.3
6	2.5×10^{-09}	2.2×10^{-09}	9.6×10^{-09}	14.7
5 – low V	1.8×10^{-09}	8.3×10^{-10}	2.1×10^{-09}	21.8
5 – high V	7.1×10^{-10}	4.3×10^{-10}	1.7×10^{-09}	21.8
4	2.8×10^{-09}	2.4×10^{-09}	7.2×10^{-09}	15.0
3	2.0×10^{-09}	1.7×10^{-09}	2.5×10^{-09}	10.2

Notes. The lower and upper bound of parameter range covering 67% of the probability density for this value considering the probability distributions of the C_2H and H_2 column densities. The column density values are taken from Table 6 of Mangum et al. (2019).

detected transitions is 41.9 K and thus we should not be sensitive to changes in temperature much above this value. Mangum et al. (2019) also found temperatures >50 K on scales similar to the GMCs using measurements of H_2CO emission.

On the other hand, the gas densities are relatively well constrained and consistent with other measurements in the region. At $\sim 10^5$ cm^{-3}, the gas density is similar to the high end of the range found using dust masses from Sakamoto et al. (2011) and the values measured at higher resolution by Leroy et al. (2018) also from dust.

4. The origin of C_2H in the NGC 253 GMCs

In the previous section, column densities were derived for each GMC, excluding the extended emission. In this section, those column densities and the corresponding fractional abundances are used to constrain chemical models to investigate the origin of C_2H in these clouds.

4.1. PDR chemistry

C_2H is ubiquitous in galactic PDRs (Lucas & Liszt 2000) and so we explore the possibility that the observed emission arises from the low A_v outer edges of the GMCs. Therefore, a grid of PDR models was run using UCL_PDR[5] (Bell et al. 2006; Priestley et al. 2017), a code that has been extensively benchmarked (Röllig et al. 2007). In these models, a 1D cloud of gas in equilibrium was considered with a variety of physical parameters given in Table 7 assuming a uniform density. The model iteratively solves the temperature and chemistry considering a variety of heating and cooling processes as well as 215 chemical

---

[5] https://uclchem.github.io/ucl_pdr

Table 7. Parameters varied for PDR chemical model.

Variable	Symbol	Range
Gas density	n_{H2}	10^4–10^6 cm^{-3}
External radiation field	G	1–10^5 Habing
Cosmic-ray ionization rate	ζ	$1, 10^3\ \zeta_0$

Notes. $\zeta_0 = 1.3 \times 10^{-17}$ s^{-1}.

species interacting through ~ 2900 reactions until an equilibrium is reached.

The model produces fractional abundances as a function of distance into the GMC or, equivalently, visual extinction. Therefore, the species' column densities can also be calculated by limiting the model to the maximal H_2 column density measured towards the region and integrating the C_2H density over that range.

The fractional abundance of C_2H as a function of depth in these models is given in Fig. 6. The key result is that whilst many models reach C_2H abundances compatible with those measured in NGC 253 at low A_v, none are capable of explaining the observed column density of $\sim 10^{15}$ cm^{-2} if a uniform medium is assumed. In fact, assuming a maximum H_2 column density of 2.2×10^{24} cm^{-2} (the largest measured by Mangum et al. 2019 towards one of the GMCs discussed here), the largest possible C_2H column density from a model with the canonical Milky Way cosmic-ray ionization rate of $\zeta_0 = 1.3 \times 10^{-17}$ s^{-1} is 6×10^{13} cm^{-2}. This is over an order of magnitude too low to match any GMC.

This is because the abundance reduces with depth into the cloud so only the outer edges contribute to the column. One solution to this would be to invoke clumpiness. However, for PDR chemistry to be responsible for the observed C_2H emission, the
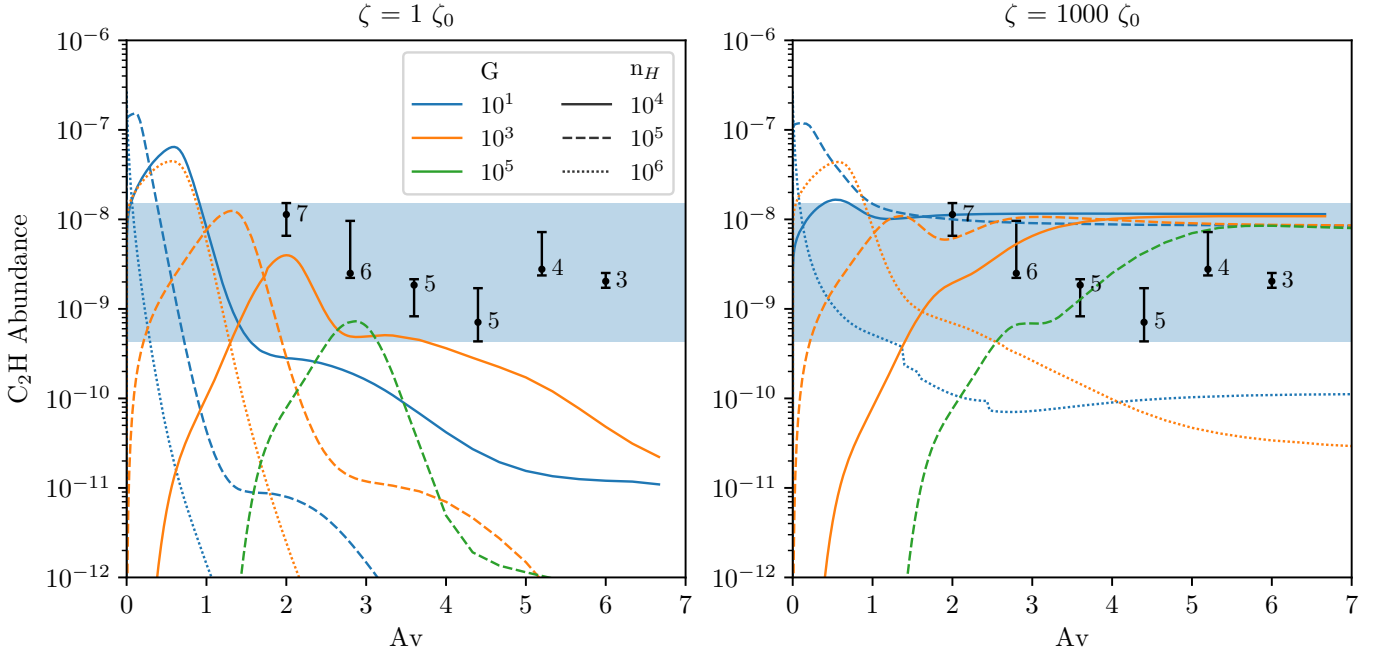
Fig. 6. Fractional abundance as a function of depth into the cloud from PDR modeling and observations. The depth into the cloud is given as the equivalent visual extinction. The black dots are numbered according to the GMC they represent and error bars show the observed abundance towards that GMC, their position on the x-axis is arbitrary and does not represent the cloud sizes. The lines show UCL_PDR models with different parameters. The shaded band covers the abundance range of all GMC measurements. In the low cosmic-ray ionization rate models (*left*), the abundance decreases with distance into the cloud so the total column density is less than the observed column density despite the high abundances reached at low A_v.

average A_v would need to be less than 2 mag despite the fact the column density in these clouds would give an $A_v > 500$ mag.

If, on the other hand, an enhanced cosmic-ray ionization rate is introduced, the model abundances of C_2H become enhanced and constant with respect to A_v. This enhancement is due to the high ionization rate creating an environment where the ionization fraction is high, much like a PDR, even in high A_v regions of the model. In the models, C_2H is produced primarily through the chain,

1. $C^+ + CH_2 \longrightarrow C_2H^+ + H$
2. $H_2 + C_2H^+ \longrightarrow C_2H_2^+ + H$
3. $C_2H_2^+ + e^- \longrightarrow C_2H + H$

regardless of whether C^+ is produced through photochemistry or cosmic ray ionization. For a rate of 1000 ζ_0, many models give a C_2H abundance of $\sim 10^{-8}$ regardless of depth into the cloud. This produces column densities in line with those observed. Therefore, ruling out the possibility that the GMCs are so clumpy that the average visual extinction is less than 2 mag, it can be concluded that the C_2H emission observed in NGC 253 does not primarily originate from the PDR regions in the clouds. If that is the case, the C_2H emission must come from within the clouds where some process maintains the C_2H abundance at high visual extinctions and this is explored in the following sections.

4.2. Dense cloud chemistry

Given the likelihood that C_2H emission observed towards the GMCs in NGC 253 comes from within those clouds rather than the UV irradiated skin, it becomes appropriate to model the chemistry with a dense cloud model where photo-processes are assumed to be negligible. UCLCHEM[6], a gas-grain chemical code (Holdship et al. 2017) was used for this purpose.

Table 8. Parameters varied for dark cloud chemical model.

Variable	Symbol	Range
Gas density	n_{H2}	$10^4 - 10^6$ cm^{-3}
Gas temperature	T_g	$50 - 300$ K
Cosmic-ray ionization rate	ζ	$10 - 10^6\ \zeta_0$

Notes. $\zeta_0 = 1.3 \times 10^{-17}$ s^{-1}.

It is assumed that since the extinction of UV photons is the only depth dependent process, the entire interior of a GMC can be modeled as a single point with an A_v that is sufficiently high to make all UV processes negligible. Therefore, a grid of single point models was run with an A_v of 10 mag which is sufficient to reduce the local UV field in the model to zero. This grid covered a range of gas densities, temperatures, and cosmic-ray ionization rates to represent different GMC conditions which are given in Table 8.

Each GMC model used initial abundances that were generated by a model that started from purely atomic gas with solar elemental abundances (Asplund et al. 2009) with silicon depleted to 1% of its solar value. The initial density was $n_{H2} = 10^2$ cm^{-3} and the density then increased according to a freefall collapse model to the required density of the GMC model. This provided realistic initial abundances for a GMC that has formed from diffuse gas without assuming values which the chemical network may not be able to produce. Each model was run for 5 Myr so that the abundance over time and the steady-state value could be analysed.

The model results in Fig. 7 show that equilibrium values are quickly reached. Note that at $t = 0$ yr, the model is already at the post-collapse density. In fact, in many cases, the C_2H abundance
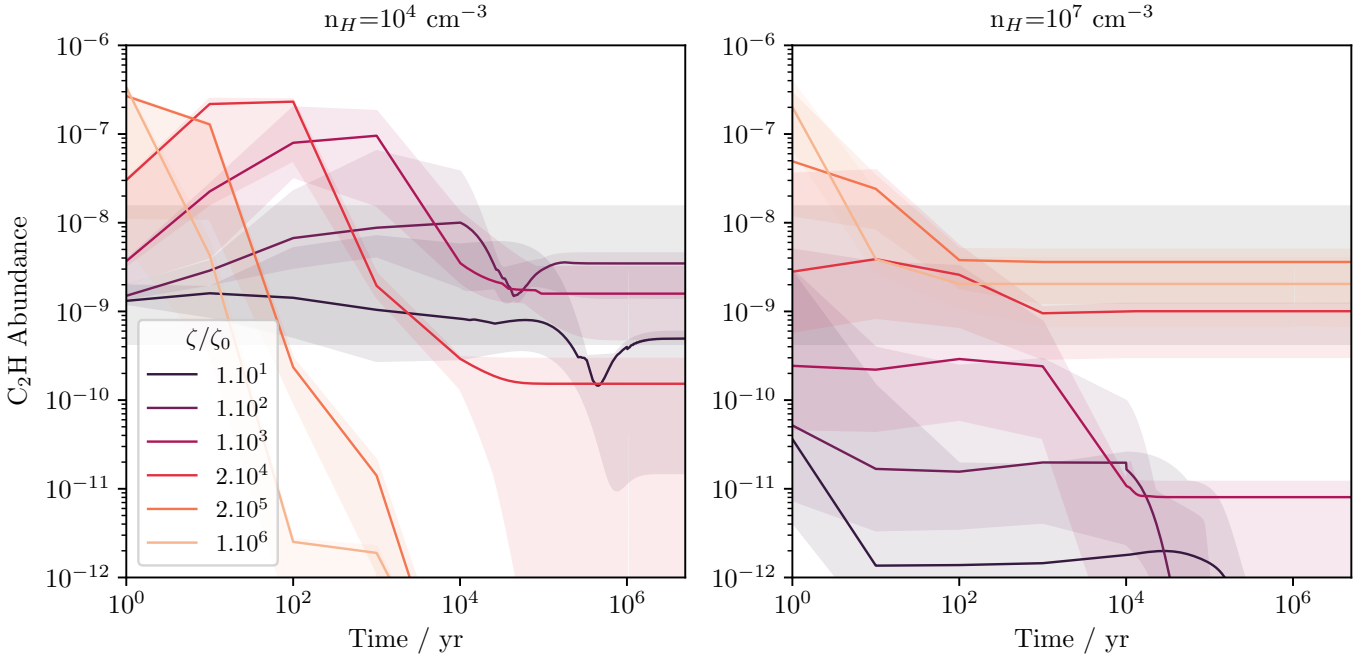
Fig. 7. Fractional abundance of C_2H as a function of time in the UCLCHEM models. Each line shows the median value of the abundance for a given cosmic-ray ionization rate as temperature is varied and the shaded regions show the minimum and maximum abundances over that temperature variation. The cosmic-ray ionization rate is given as a multiple of $\zeta_0 = 1.3 \times 10^{-17}$ s^{-1} and a sample of the lines are given in the legend. The grey shaded area shows the observed range.

becomes constant after as few as 10^4 years. Further, within the limits of the grid, the steady state abundance of C_2H is typically not strongly affected by the gas temperature. In fact, as long as the abundance of C_2H is sufficiently high to match the observations, the temperature only creates a small variance as shown by the shaded region around each line in the plot. Instead, the combination of the gas density and cosmic-ray ionization rate sets the abundance.

If it is assumed the abundances reach steady state, the cosmic-ray ionization rate required to obtain the measured C_2H abundances appears to have a log-log relationship to the density. This is to be expected given that higher densities tend to decrease the total ionization fraction in the models and so a higher cosmic-ray ionization rate is needed to maintain the PDR-like chemistry that produces C_2H. Thus, using the estimates of the gas density from Sect. 3.3.2, it may be possible to constrain the ionization rate. Figure 8 shows the steady state abundance of C_2H as a function of the gas density and cosmic-ray ionization rate. Overplotted are points representing each GMC, showing the range of densities found in Sect. 3.3.2 and the cosmic-ray ionization rate range that gives model abundances within the measured limits for that GMC.

GMC 7 presents a problem as no model produces a large enough abundance of C_2H to match even the lower limit for that GMC and hence it is missing from Fig. 8. However, there is a lot of uncertainty in both the derived fractional abundance and the chemical model. The H_2 column density used to convert to abundance was derived using an assumed dust temperature and dust to gas ratio as well as assuming optically thin dust emission. If the resulting column density was underestimated by even a factor of 2, the abundance can be fit. If we further consider uncertainties such as the initial elemental abundance of carbon in the chemical model, a discrepancy of this magnitude is unsurprising.

The poor fit of GMC 7 and the fact that the cosmic-ray ionization rate can only be constrained to within a few orders of magnitude for the other GMCs indicates that this analysis should only be considered qualitatively. The fits show that the cosmic ray ionization rate is likely to be high in these regions but the specific values are very uncertain. Each GMC has a lower limit on the cosmic-ray ionization rate of $1500 \zeta_0$ except for the high velocity component of GMC 5 where the density is poorly constrained and so ζ can be as low as $100 \zeta_0$. Overall, we can conclude that the observed C_2H emission could arise from the chemistry of a cosmic ray dominated region where the cosmic-ray ionization rate must be much higher than standard but cannot constrain it to within an order of magnitude.

4.3. Shock chemistry

Whilst the previous section indicates cosmic rays may be the main driver of the chemistry producing C_2H, it should be noted that other possibilities exist. Most importantly, the model effectively treats cosmic rays as ionization events that are not reduced by the gas column density and so other sources of ionization such as the strong X-ray irradiation in the region (Strickland et al. 2002) could be at work instead. It is also possible that physical processes such as shocks not included in the previous models could cause an enhanced abundance of C_2H.

The dense cloud modeling shows that simply heating the gas or increasing the density cannot produce enough C_2H. This is illustrated in Fig. 7 where the shaded regions show little variation in abundances as the temperature varies between 50 and 300 K and in Fig. 8 which shows the C_2H abundance actually decreases with increasing density for a given cosmic ray ionization rate. However, more complex physical processes could be at work. A natural possibility is turbulence which would affect the chemistry through shocks as low velocity shocks have previously been
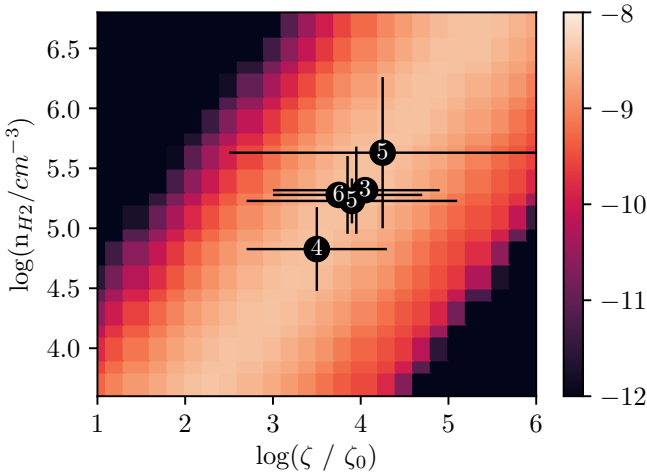
Fig. 8. Steady state C$_2$H abundance shown in colour scale as a function of gas density and cosmic-ray ionization rate in units of $\zeta_0 = 1.3 \times 10^{-17}$ s^{-1}. The values given are a median over different gas temperatures. Each point represents a GMC with the vertical lines showing the upper and lower limits on the density for that cloud. The horizontal lines span the cosmic-ray ionization rate values that give abundances within the measured range for those density values. GMC 7 does not appear on this diagram as no model produces a large enough abundance of C$_2$H to match even its observed lower-limit.

Table 9. Parameters varied for shock chemical models.

Variable	Symbol	Range
Gas density	n_{H2}	$10^4 - 10^6$ cm^{-3}
Gas temperature	T_{g}	$10 - 50$ K
Cosmic-ray ionization rate	ζ	$1 - 10\ \zeta_0$
Shock velocity	V_{s}	$5 - 40$ km s^{-1}

Notes. $\zeta_0 = 1.3 \times 10^{-17}$ s^{-1}.

found to dominate the heating in the region (Martín et al. 2006). These shocks would tend to heat and compress the gas as well as remove material from the grains. Furthermore, in NGC 1068 it was found one possible cause of the high C$_2$H abundances was in fact shocks (Aladro et al. 2013; García-Burillo et al. 2017).

To explore this, we run a simple grid of shock models using UCLCHEM's shock module based on the C-shock parametrization of Jiménez-Serra et al. (2008). We vary the shock velocity from 5 to 40 km s^{-1}, to trial a range of velocities over which the shock treatment is applicable. We apply these shocks to gas with pre-shock densities between 10^4 and 10^6 cm^{-3} with initial abundances taken from a collapse model as described in Sect. 4.2. We vary the pre-shock gas temperature from 10 to 50 K and cosmic-ray ionization rate between 1 and 10 ζ_0 to separate the effects of shocks and high ionization rates. These parameter ranges are summarized in Table 9.

In almost every model, the pre-shock C$_2$H abundance was an order of magnitude too low to match observations and the passage of a shock permanently reduced the C$_2$H abundance, meaning most shocks could not reproduce observations. However, a small subset of shock models with a density of 10^4 cm^{-3} and a shock velocity greater than 20 km s^{-1}, had C$_2$H abundances that were enhanced briefly by the shock passage. In each of these models, there is a short period of $\sim 10^5$ years where the C$_2$H abundance is enhanced to the levels observed in NGC 253 (see Fig. 9).
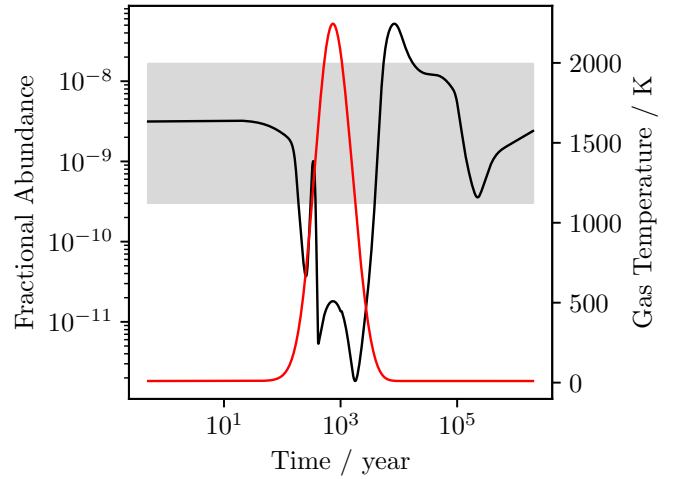

Fig. 9. Fractional abundance of CCH through time for a 20 km s^{-1} shock propagating through gas with a pre-shock density of 10^4 cm^{-3} plotted in black, temperature through the shock plotted in red. The range of observed C$_2$H abundances is shown in grey.

Naturally, a single simple shock model is difficult to apply to a large cloud that is possibly experiencing multiple small shocks due to turbulent internal motion. However, taking an average over the shock structure, the model abundances of this subset of shock models are all within the lower and upper bounds on the C$_2$H abundance for at least one GMC as given in Table 7. Therefore, if one argues that shocks are so ubiquitous in these GMCs that almost all of the gas is constantly in a state of having just been shocked (within 10^5 years) then the overall average C$_2$H abundance will be within our observational constraints.

However, there are several aspects of the GMCs that indicate the required shock conditions are not met in these objects. Our models indicate shocks with a velocity greater than 20 km s^{-1} are necessary but previous work has suggested shocks (<20 km s^{-1}) are common in the region (García-Burillo et al. 2000; Martín et al. 2006). Moreover, the post shock density in these models is only 5×10^4 cm^{-3} and the gas densities in the GMCs are larger. This is vital as models with higher pre-shock gas densities do not reproduce the observed abundances. Finally, it is unlikely that all of the gas in the GMCs is shocked repeatedly on a timescale of 10^5 years but averaging over longer times in the shock model produces abundances that are lower than those observed.

To summarize, a subset of shock models could potentially reproduce the abundances of C$_2$H observed in these clouds and therefore cannot be ruled out. However, the conditions required do not match those measured for the GMCs and the gas would have to be almost constantly undergoing a shock. Therefore, we consider it unlikely in comparison to the wide range of cosmic ray dominated models that fit the measured abundances.

4.4. Relationship to other sources

In the Milky Way, it is typical to observe C$_2$H with abundances similar to those measured for NGC 253 in PDRs. However, it is clear from the modeling done in this work that it cannot be the case that C$_2$H in NGC 253 arises entirely from PDRs. The observed column densities are far too high and another process must be at play.

In this work, we have proposed that a large degree of ionization, likely from cosmic rays, is responsible for the C_2H abundance or, less likely, ubiquitous shocks in the GMC. This is similar to the molecular cloud G+0.693−0.027 which has a C_2H abundance of 4×10^{-8} (Bizzocchi et al. 2020). The cosmic ray ionization rate is expected to be several orders of magnitude higher than the standard Milky Way value at the Galactic centre. However, the chemistry in the cloud is also thought to be shock dominated (Requena-Torres et al. 2006).

A comparison to NGC 1068 is also of interest. In that galaxy, the C_2H emission was observed towards both the starburst ring and along the AGN driven outflow. However, only the $N = 1-0$ transition was observed by García-Burillo et al. (2017) and so the column density could not be well constrained. Assuming temperatures around 50 K and LTE, a fractional abundance of C_2H similar to that measured here for NGC 253 can be recovered for the starburst ring. However, a true comparison of the star forming regions in these galaxies would require higher N transitions of C_2H to be observed toward NGC 1068 as the majority of emission from the GMCs in NGC 253 was found in those lines.

C_2H was also detected in NGC 1068 at higher abundances in the range 10^{-7} to 10^{-6} around the AGN driven outflow. A variety of physical factors including high UV fields, high cosmic-ray ionization rates and shocks could all produce this abundance for a very short time according to chemical modeling work in García-Burillo et al. (2017). As a result, the authors conclude the high abundances are maintained by a dynamic environment around the outflow in which gas is constantly resupplied to the interface between the outflow and its surroundings. As a result, a pseudo-steady state is reached where the gas is well fit by the early stages of their chemical models. Whilst this picture makes sense for an outflow interface, it does not apply to the GMCs observed in NGC 253 which are much more static.

Thus, we are tracing fundamentally different gas in each galaxy with C_2H. This is evidenced by the fact the majority of the C_2H emission does not appear to follow the outflow of NGC 253 as traced in CO by Krieger et al. (2019). In fact, only the $N = 1-0$ line traces the base of the outflow as found in previous work (Meier et al. 2015) unlike in NGC 1068 where is traces a large extend of the outflow (García-Burillo et al. 2017). This lack of outflow emission indicates that the energetic processing producing the high abundance of C_2H in NGC 1068's AGN driven outflow is not present in NGC 253's starburst driven outflow. NGC 253 appears to represent a third class of C_2H rich gas in which an ionizing process such as cosmic ray ionization maintains an ion dominated chemistry and therefore enhanced abundances of C_2H well into dark regions. It is clearly distinguishable from the outflow case by its lower C_2H abundance and coincidence with dense gas but differentiated from PDR emission by its high column density.

5. Conclusions

The emission of the $N = 1-0$ to $N = 4-3$ rotational transitions of C_2H in NGC 253 was imaged with ALMA at a resolution of 28 pc (1.6″). Most of the C_2H emission traces the dense gas of the brightest GMCs that have been previously studied in the CMZ of NGC 253. However, the emission from the $N = 1-0$ transition also traces diffuse gas in the CMZ itself. C_2H does not appear to follow the galaxy's starburst driven outflow.

Spectral modeling was used to infer the gas properties of the GMCs. The temperatures were found to be >50 K and the gas densities varied from 10^5 cm^{-3} to 10^6 cm^{-3}. These values are

in line with those previously measured in the GMCs. The column density of C_2H was also constrained to be in the range $10^{15}-10^{16}$ cm^{-2} which corresponds to fractional abundances $\sim 10^{-9}$.

Chemical modeling showed that despite being enhanced in PDRs, the C_2H emission in these GMCs could not entirely arise from the photon dominated outer regions of these dense clouds but must instead come from within the clouds. C_2H in these GMCs most likely arises from gas where the ionization fraction is kept high by some ionizing process such as cosmic rays. Alternatively, ubiquitous shocks could be responsible for the measured C_2H abundance but this would require the entire gas to be shocked on such a short timescale that this is unlikely.

If a high cosmic-ray ionization rate is responsible for the C_2H abundance, the ionization rate in each GMC is constrained to within a few orders of magnitude only. The values for each GMC vary from 10^3 to 10^6 ζ_0. A more sensitive probe of the cosmic-ray ionization rate should be utilized in these regions to confirm the presence of a high ionization rate and better constrain its value.

References

Aladro, R., Martín, S., Martín-Pintado, J., et al. 2011, A&A, 535, A84
Aladro, R., Viti, S., Bayet, E., et al. 2013, A&A, 549, A39
Aladro, R., Martín, S., Riquelme, D., et al. 2015, A&A, 579, A101
Ando, R., Nakanishi, K., Kohno, K., et al. 2017, ApJ, 849, 81
Asplund, M., Grevesse, N., Sauval, A. J., & Scott, P. 2009, ARA&A, 47, 481
Astropy Collaboration (Robitaille, T. P., et al.) 2013, A&A, 558, A33
Astropy Collaboration (Price-Whelan, A. M., et al.) 2018, AJ, 156, 123
Bell, T. A., Hartquist, T., Viti, S., & Williams, D. A. 2006, A&A, 459, 805
Bizzocchi, L., Prudenzano, D., Rivilla, V. M., et al. 2020, A&A, 640, A98
Bolatto, A. D., Warren, S. R., Leroy, A. K., et al. 2013, Nature, 499, 450
Cuadrado, S., Goicoechea, J. R., Pilleri, P., et al. 2015, A&A, 575, A82
Dagdigian, P. J. 2018, MNRAS, 479, 3227
Dahlem, M., Weaver, K. A., & Heckman, T. M. 1998, ApJS, 118, 401
Foreman-Mackey, D., Hogg, D. W., Lang, D., & Goodman, J. 2013, PASP, 125, 306
García-Burillo, S., Martín-Pintado, J., Fuente, A., & Neri, R. 2000, A&A, 355, 499
García-Burillo, S., Viti, S., Combes, F., et al. 2017, A&A, 608, A56
Holdship, J., Viti, S., Jiménez-Serra, I., Makrymallis, A., & Priestley, F. 2017, AJ, 154, 38
Hsieh, T. H., Lai, S. P., Belloche, A., Wyrowski, F., & Hung, C. L. 2015, ApJ, 802, 126
Jiménez-Serra, I., Caselli, P., Martín-Pintado, J., & Hartquist, T. 2008, A&A, 482, 549
Krieger, N., Bolatto, A. D., Walter, F., et al. 2019, ApJ, 881, 43
Krieger, N., Bolatto, A. D., Leroy, A. K., et al. 2020, ApJ, 897, 176
Leroy, A. K., Bolatto, A. D., Ostriker, E. C., et al. 2015, ApJ, 801, 25
Leroy, A. K., Bolatto, A. D., Ostriker, E. C., et al. 2018, ApJ, 869, 126
Lucas, R., & Liszt, H. S. 2000, A&A, 358, 1069
Mangum, J. G., Ginsburg, A. G., Henkel, C., et al. 2019, ApJ, 871, 170
Martín, S., Mauersberger, R., Martín-Pintado, J., Henkel, C., & García-Burillo, S. 2006, ApJS, 164, 450
Martín, S., Martín-Pintado, J., Blanco-Sánchez, C., et al. 2019, A&A, 631, A159
Martín, S., Mangum, J. G., & Harada, N. 2021, A&A, submitted, https://doi.org/10.1051/0004-6361/202141567
Meier, D. S., & Turner, J. L. 2005, ApJ, 618, 259
Meier, D. S., Walter, F., Bolatto, A. D., et al. 2015, ApJ, 801, 63

Pickett, H. M. 1998, Appl. Opt., 24, 2235
Pilleri, P., Treviño-Morales, S., Fuente, A., et al. 2013, A&A, 554, A87
Priestley, F., Barlow, M. J., & Viti, S. 2017, MNRAS, 472, 4444
Rekola, R., Richer, M. G., McCall, M. L., et al. 2005, MNRAS, 361, 330
Requena-Torres, M. A., Martín-Pintado, J., Rodríguez-Franco, A., et al. 2006, A&A, 455, 971
Röllig, M., Abel, N. P., Bell, T. A., et al. 2007, A&A, 467, 187
Sakamoto, K., Mao, R. Q., Matsushita, S., et al. 2011, ApJ, 735, 19
Schöier, F. L., van der Tak, F. F. S., van Dishoeck, E. F., & Black, J. H. 2005, A&A, 432, 369
Strickland, D. K., Heckman, T. M., Weaver, K. A., Hoopes, C. G., & Dahlem, M. 2002, ApJ, 568, 689
Turner, B. E., Terzieva, R., & Herbst, E. 1999, ApJ, 518, 699

van der Tak, F. F. S., van Dishoeck, E. F., Evans, N. J., II, & Blake, G. A. 2000, ApJ, 537, 283
van der Tak, F. F. S., Black, J. H., Schöier, F. L., Jansen, D. J., & van Dishoeck, E. F. 2007, A&A, 468, 627
Vastel, C., Bottinelli, S., Caux, E., Glorian, J. M., & Boiziot, M. 2015, in SF2A-2015: Proceedings of the Annual Meeting of the French Society of Astronomy and Astrophysics, eds. F. Martins, S. Boissier, V. Buat, L. Cambrésy, & P. Petit, 313
Walter, F., Bolatto, A. D., Leroy, A. K., et al. 2017, ApJ, 835, 265
Watt, G. D., White, G. J., Millar, T. J., & van Ardenne, A. 1988, A&A, 195, 257
Wootten, A., Bozyan, E. P., Garrett, D. B., Loren, R. B., & Snell, R. L. 1980, ApJ, 239, 844

Appendix A: SpectralRadex

A.1. Package description

SpectralRadex[7] is a Python module that was created in the process of this work and is now generally available through github[8] and Pypi. As such it is described here in detail.

The module comprises two parts: a wrapper for RADEX (van der Tak et al. 2007) and a spectral modeling library. Whilst many packages exist for the former purpose, most either compile the original RADEX source code including Fortran 77 COMMON blocks using numpy's F2PY or create an interface for calling the compiled RADEX binary. The former has less I/O overhead and should be preferred but the use of COMMON blocks means no copies of the program can be run simultaneously and is therefore problematic for multiprocessing. SpectralRadex solves this issue by rewriting the RADEX source code, updating it to modern Fortran standards and dropping common blocks in favour of Fortran modules before compiling with F2PY.

For the latter purpose, SpectralRadex makes use of RADEX to produce non-LTE spectra from RADEX inputs, a set of frequencies at which to evaluate the intensities and the velocity by which all lines should be shifted. The formalism for this is detailed below and borrows heavily from CASSIS (Vastel et al. 2015).

A.2. Spectral modeling Formalism

In order to calculate the emission from a single molecular transition as a function of frequency, the excitation temperature and the optical depth are required. The brightness temperature is given by,

$$T_B = [J_\nu(T_{ex}) - J_\nu(T_{BG})](1 - \exp(-\tau_\nu)) \tag{A.1}$$

where J_ν is the radiation temperature, T_{ex} is the excitation temperature, T_{BG} is the background temperature, and τ_ν is the optical depth as a function of velocity. The radiation temperature is simply,

$$J_\nu(T_{ex}) = \frac{\frac{h\nu}{k}}{\exp\frac{h\nu}{kT_{ex}} - 1} \tag{A.2}$$

where ν is the frequency, h is Planck's constant and k is Boltzmann's constant. The optical depth, can then be calculated by converting frequency to equivalent velocity shift using the rest frequency of the transition and then assuming a Gaussian line profile

$$\tau_\nu = \tau_0 e^{\left(-4\ln(2)\frac{(\nu-\nu_0)^2}{\Delta\nu^2}\right)} \tag{A.3}$$

where τ_0 is the optical depth at line centre, ν_0 is the velocity shift of the emission, and $\Delta\nu$ is the FWHM of the line. Thus all that is required is to calculate T_{ex} and τ_0 for a given transition and set of physical parameters.

This can be achieved through the use of RADEX. For a given set of physical parameters RADEX will provide the optical depth at line centre for every transition and the excitation temperature that gives the correct brightness temperature at line centre. Thus, a non-LTE spectrum can be generated by taking these quantities from an appropriate RADEX model. In the high density limit, this tends to the LTE solution but at lower densities it can deviate significantly.

In SpectralRadex, T_B is calculated as a function of frequency for each line and then combined to give the overall spectrum of the molecule. Where lines overlap, SpectralRadex follows Hsieh et al. (2015) and uses an opacity weighted radiation temperature:

$$T_B = \left(\frac{\Sigma_i J\nu(T_{ex}^i)\tau_\nu^i}{\Sigma_i \tau_\nu^i} - J_\nu(T_{BG})\right)(1 - \exp(-\tau_\nu)). \tag{A.4}$$

---

[7] https://spectralradex.readthedocs.io
[8] https://github.com/uclchem/SpectralRadex

Appendix B: The other fits

In this section, the best fit models for each of the GMC spectra are shown except for GMC 5 which is shown in Figure 5. Figure B.1 shows GMC7, Figure B.2 shows GMC 6 and Figure B.3 shows the best fit to GMC 4.
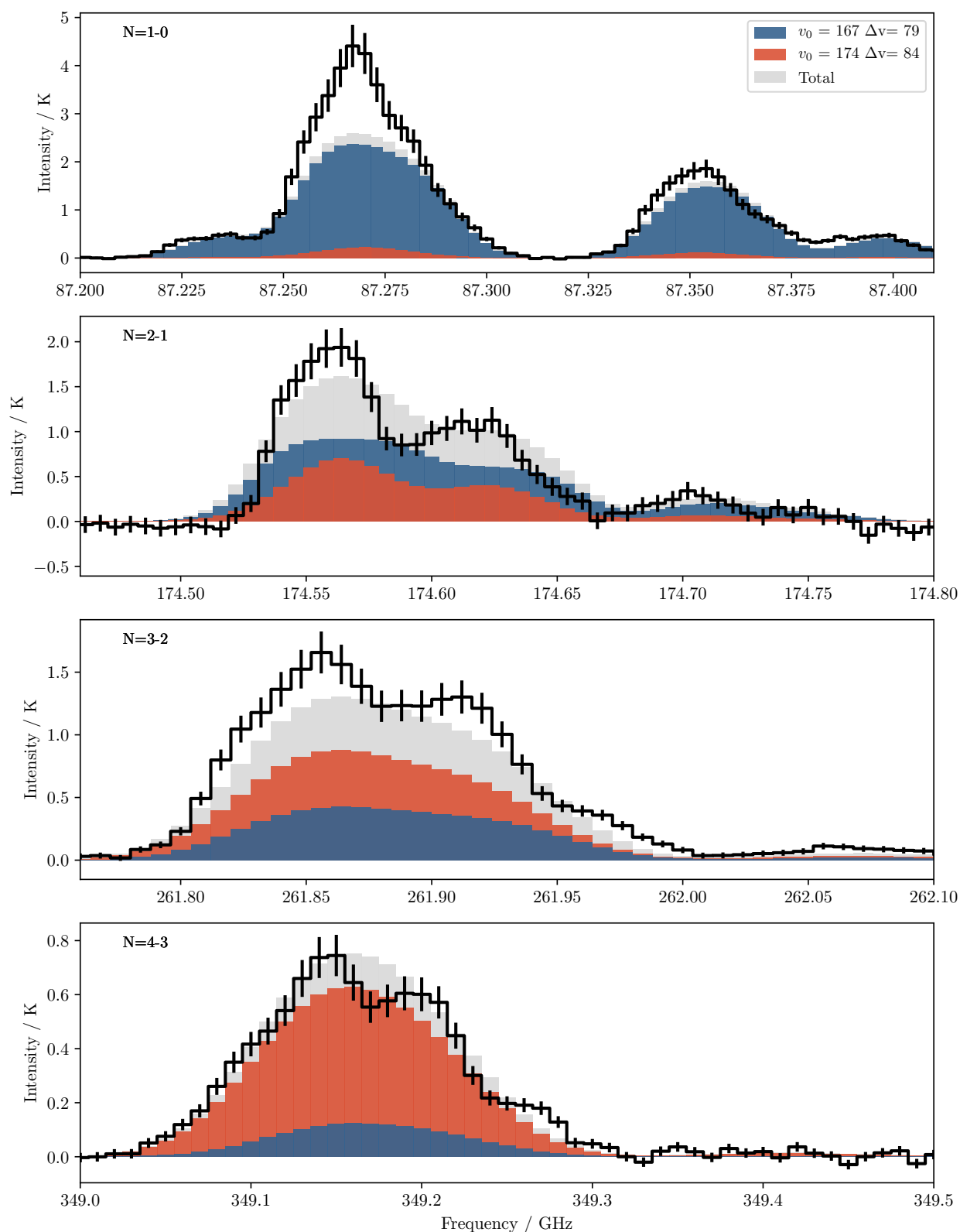

Fig. B.1. Measured spectrum from GMC 7 in black with error bars. Model spectra generated from most likely values for GMC 7 as filled histograms. The blue component shows the low density extended emission, the red shows the high density GMC emission, and the grey shows the complete model.
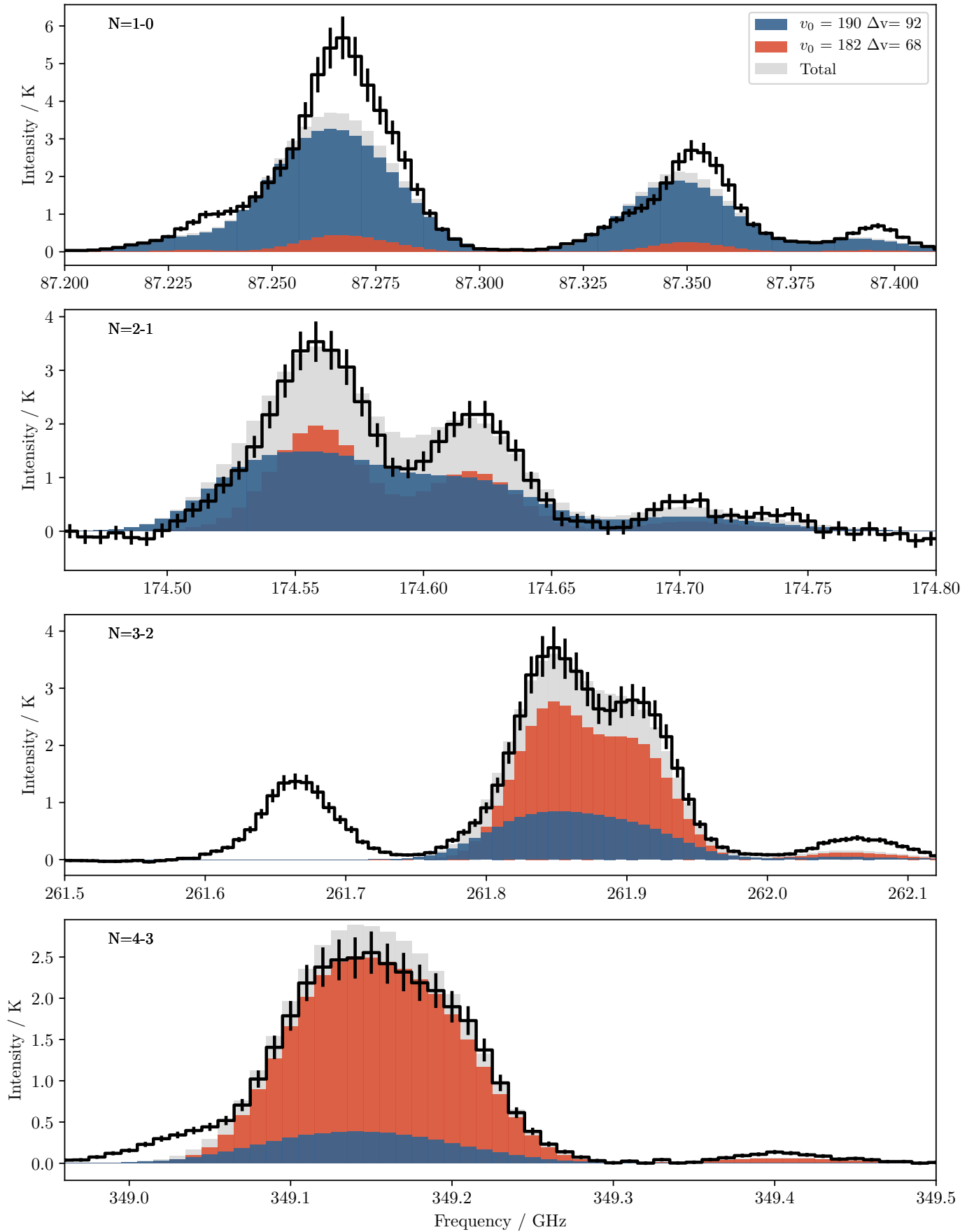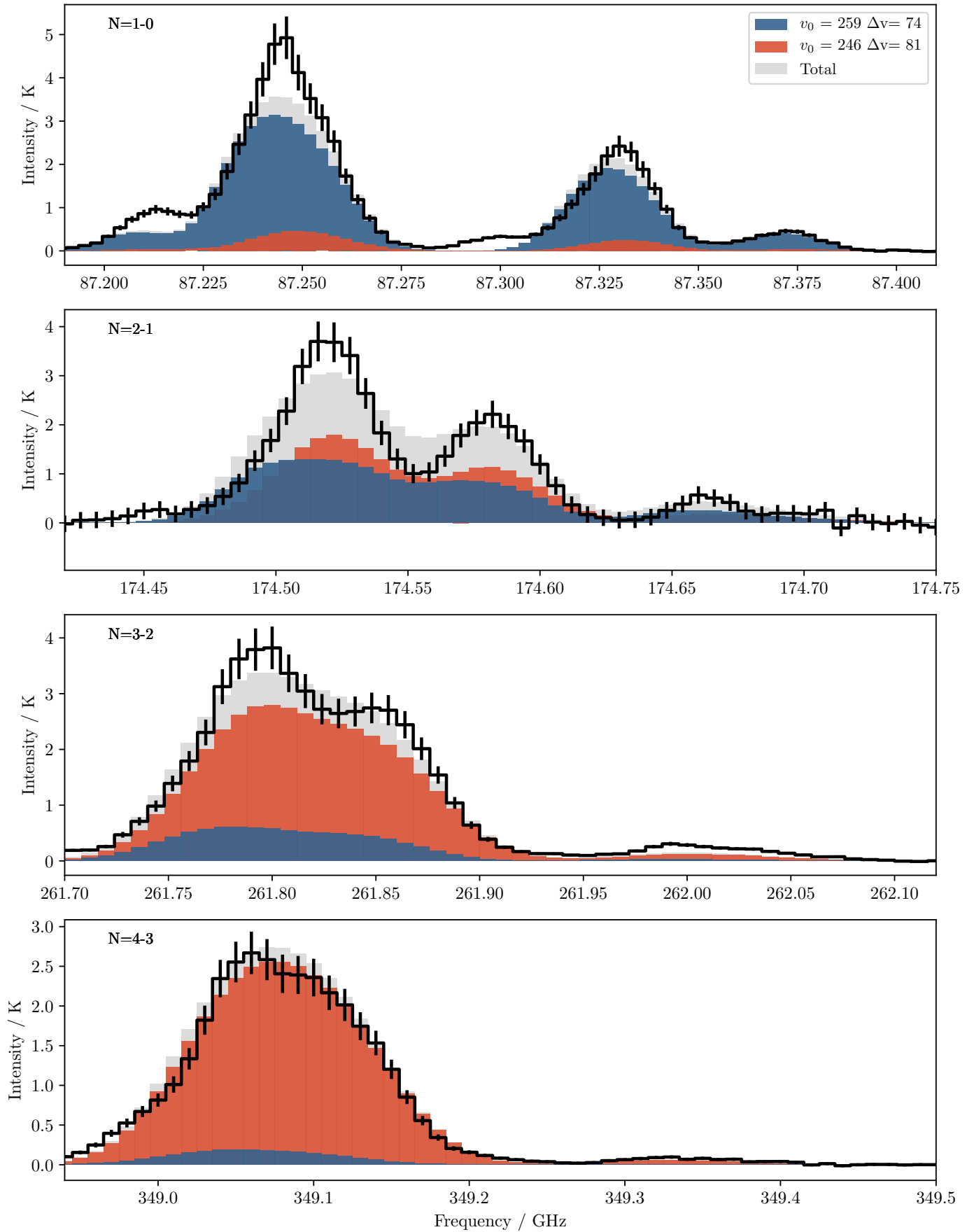
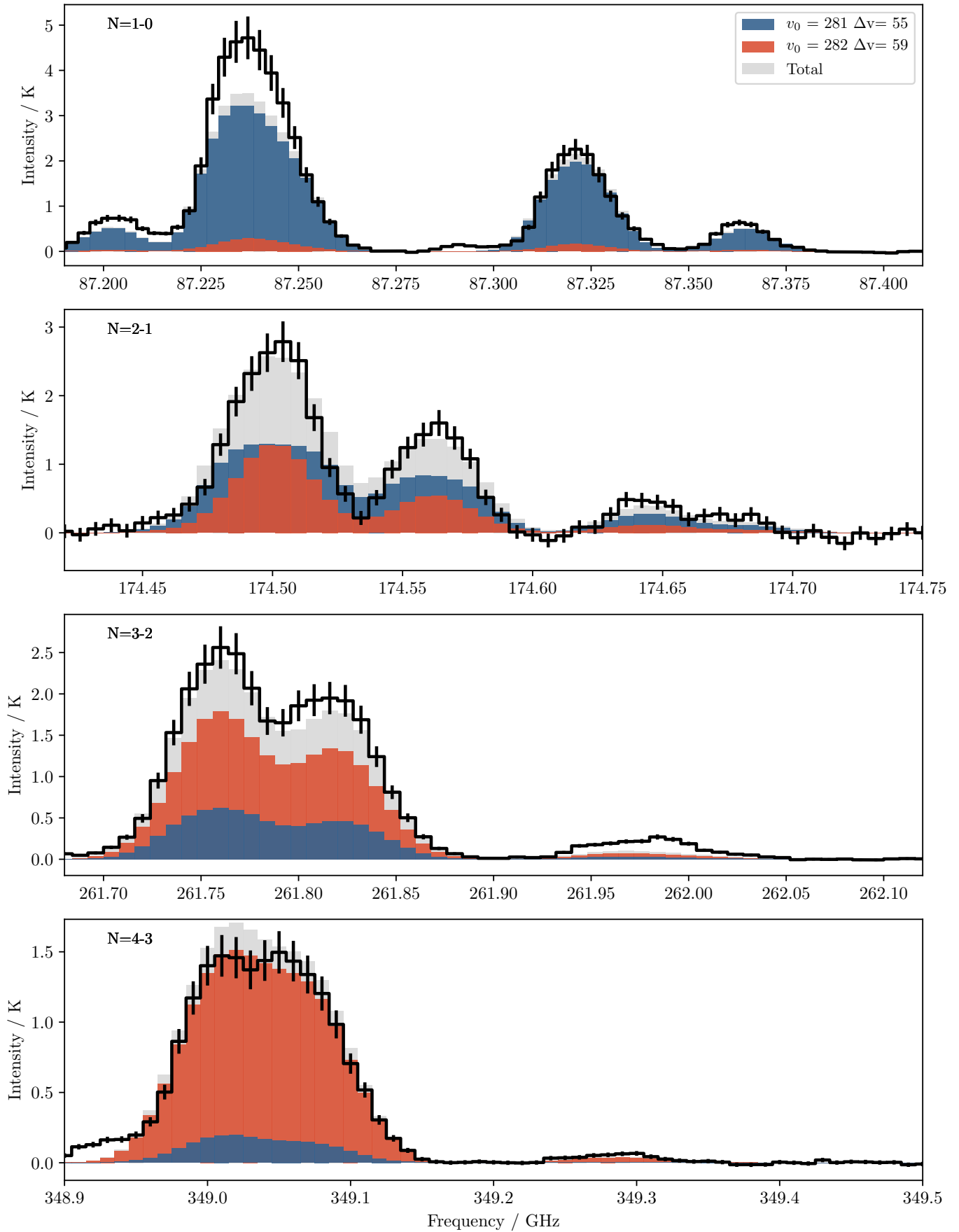**Fig. B.2.** Similar to Figure B.1 for GMC 6.

Fig. B.3. Similar to Figure B.1 for GMC 4.

Fig. B.4. Similar to Figure B.1 for GMC 3.